nature physics

ARTICLES

PUBLISHED ONLINE: XX MONTH XXXX | DOI: 10.1038/NPHYS3927

Long-range mutual synchronization of spin Hall nano-oscillators

A. A. Awad[1], P. Dürrenfeld[1], A. Houshang[1], M. Dvornik[1], E. Iacocca[1], R. K. Dumas[1] and J. Åkerman[1,2]★

The spin Hall effect in a non-magnetic metal with spin–orbit coupling injects transverse spin currents into adjacent magnetic layers, where the resulting spin transfer torque can drive spin wave auto-oscillations. Such spin Hall nano-oscillators (SHNOs) hold great promise as extremely compact and broadband microwave signal generators and magnonic spin wave injectors. Here we show that SHNOs can also be mutually synchronized with unprecedented efficiency. We demonstrate mutual synchronization of up to nine individual SHNOs, each separated by 300 nm. Through further tailoring of the connection regions we can extend the synchronization range to 4 μm. The mutual synchronization is observed electrically as an increase in the power and coherence of the microwave signal, and confirmed optically using micro-Brillouin light scattering microscopy as two spin wave regions sharing the same spectral content, in agreement with our micromagnetic simulations.

Spin transfer torque (STT)[1–3] from a spin-polarized current can inject high-amplitude spin waves[4,5] in magnonic circuits based on so-called nano-contact spin torque oscillators (STNOs)[6–13]. As the wavelength of the injected spin waves is proportional to the size of the nano-contact[14], truly nanoscopic, dipolar-exchange-dominated[15] spin waves with a highly directional[16–18] nature can be generated. With the recent advent of the spin Hall effect (SHE)[19–21] substantial STT can also be exerted on a single ferromagnetic layer via a pure transverse spin current generated by a lateral current in an adjacent non-magnetic layer with spin–orbit coupling. The corresponding microwave signal generators, so-called spin Hall nano-oscillators (SHNOs)[22–27], exhibit a number of advantages compared to STNOs, such as easier nano-fabrication, reduced current through the magnetic layers, and direct optical access to the magnetodynamically active area.

The high nonlinearity[28] of STNOs can promote spin-wave-mediated mutual[29–32] and driven[33] synchronization of multiple nano-contacts[29,30,32,33]. Whereas SHNOs show a similar nonlinearity, are readily injection-locked to external microwave currents[34], and have been numerically predicted to exhibit mutual synchronization[35], any experimental demonstration is still lacking. A particular limitation of the SHNOs studied to date is the self-localized nature of the dominant mode, which cuts off spin-wave-mediated interactions. Although nanoconstriction SHNOs show signs of a second, more extended mode[25], they have primarily been studied with their magnetization in the plane, where it is known from STNOs that even the inherently propagating mode suffers localization from the magnetic field landscape[16,17]. To reduce this localization[36], we here study multiple nanoconstriction SHNOs in out-of-plane fields. We observe strong and robust mutual synchronization of as many as nine independent nanoconstrictions, each separated from its neighbour by 300 nm. Similarly, in double-constrictions with the same geometry, we demonstrate mutual synchronization for separations up to 1.2 μm. Finally, by reducing the width of the regions connecting the two nanoconstrictions we can use the negative damping from the sub-critical current density to extend the synchronization up to separations as large as 4 μm.

Figure 1 summarizes the basic structural and electrical properties of our SHNOs (see Methods). Figure 1a schematically presents the material stack, the device layout, and the applied field vector, Fig. 1b shows a scanning electron microscope (SEM) picture of a SHNO with nine nanoconstrictions ($w = 120$ nm wide and separated by $d_{cc} = 300$ nm), and Fig. 1c shows a spatial map of the lateral charge current density in the Pt layer, to which the transverse spin current entering the NiFe layer is proportional. As shown in Fig. 1d, the device resistance increases linearly with the number of constrictions; each 120 nm constriction adds 39 Ω, while the additional series resistance is 70 Ω. The in-plane angular dependence of the magnetoresistance (MR versus φ) can be fitted well (inset of Fig. 1d) by an expression based on anisotropic magnetoresistance (AMR) with a weak in-plane anisotropy of about 80–130 Oe along the length of the nanoconstrictions.

The polar field angle $\theta = 80^\circ$ was chosen to achieve positive nonlinearity in the nanoconstriction region, which is expected to reduce the localization of the auto-oscillations[28,37,38]. The in-plane angle was $\varphi = 22^\circ$–26° (except in Fig. 6) to realize sufficient electrical sensitivity to angular deflections (that is, auto-oscillations) of the magnetization.

Figure 2a shows the current dependence of the microwave electrical signal generated by a single nanoconstriction in a magnetic field of 0.72 T, tilted $\theta = 80^\circ$ out-of-plane, with its in-plane component being tilted 66° away from the current direction ($\varphi = 24^\circ$). At low currents, the signal is weak and exhibits the same redshifting current dependence as for in-plane fields[25]. At intermediate currents, the frequency shows a clear minimum above which the frequency blueshifts, the microwave power increases (Fig. 2a(II,III)), and the linewidth shows a non-monotonic behaviour (Fig. 2a(IV)). Measurements on a further seven similar single nanoconstrictions are shown in Supplementary Methods Section A.

The more interesting case of double nanoconstrictions is presented in Fig. 2b–f, which summarizes our results for five different nanoconstriction separations, ranging from 300 nm to 1.2 μm (an additional set of measurements of double

[1]Physics Department, University of Gothenburg, 412 96 Gothenburg, Sweden. [2]Material Physics, School of ICT, KTH Royal Institute of Technology, Electrum 229, 164 40 Kista, Sweden. *e-mail: johan.akerman@physics.gu.se

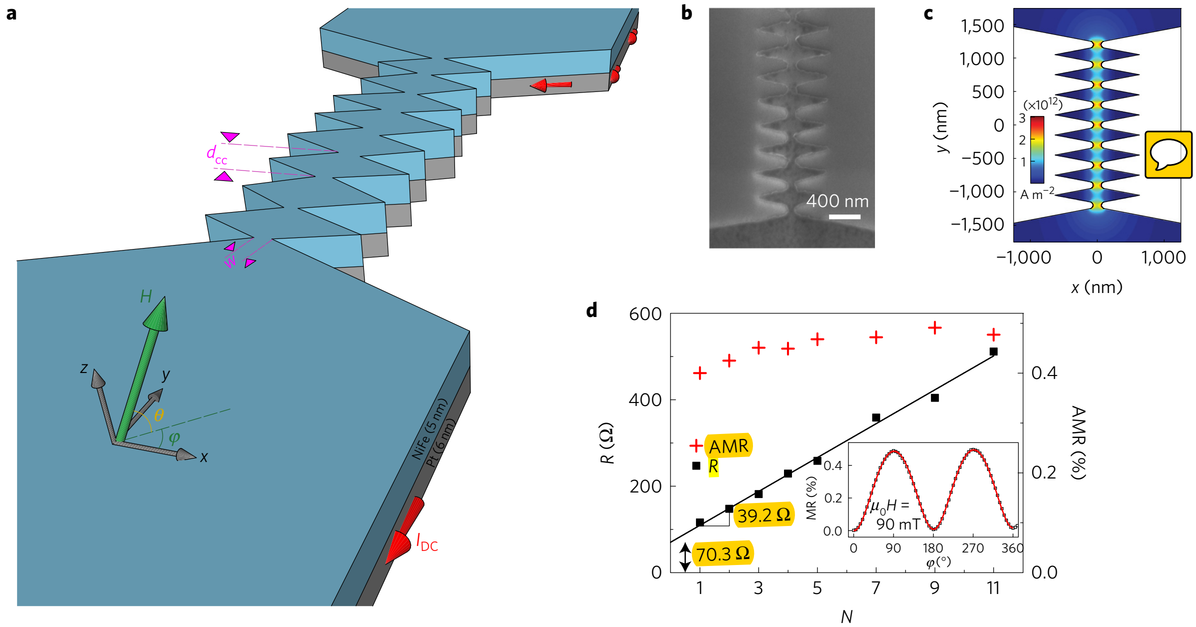

Q.2

Figure 1 | Device schematic, current distribution, and static measurements. a, A schematic illustration of the general SHNO layout, showing the patterned Py/Pt bilayer and the field and current directions used throughout the article. **b**, A scanning electron microscope (SEM) image of a SHNO with nine 120-nm-wide nanoconstrictions each separated by $d_{cc} = 300$ nm. **c**, Calculated lateral current density in the Pt layer for a total current of $I_{d.c.} = 2$ mA. **d**, Measured SHNO resistance (R) and anisotropic magnetoresistance (AMR) versus number of nanoconstrictions (N). Each nanoconstriction adds about 39 Ω. Inset: angular field scan of the resistance of a SHNO with nine nanoconstrictions showing an AMR of 0.5%. The red line is a fit allowing for a small in-plane uniaxial anisotropy field (12.9 mT) along the nanoconstrictions.

nanoconstrictions is shown in Supplementary Methods Section B). At low current, each device shows two individual and decoupled signals, with qualitatively the same behaviour as in Fig. 2a(I). The two signals can cross in frequency, as in Fig. 2c, without interference, frequency pulling or phase locking, consistent with two non-interacting auto-oscillating regions. The situation changes dramatically at higher currents, where the frequencies blueshift. For the two closest nanoconstrictions (Fig. 2b(I)), the two weak signals merge into a much stronger single signal at about 2.4 mA, indicating their mutual synchronization. This synchronized state remains stable at all higher investigated currents. At a separation of 500 nm, a current of about 3.2 mA is required for mutual synchronization; again, the synchronized state remains stable at all higher currents. At a separation of 700 nm, mutual synchronization first appears at 2.7 mA, is then broken up, until the nanoconstrictions again synchronize at about 3.3 mA. Finally, the nanoconstrictions separated by 900 nm and 1.2 μm also show clear regions of mutual synchronization, albeit for a more limited current range. At separations greater than 1.2 μm we were not able to observe synchronization in this geometry.

As expected, the mutually synchronized state is characterized by both a higher microwave power as compared to the sum of the individual SHNOs, as well as a reduced linewidth compared to the unsynchronized SHNOs[28]. In most cases, this improvement is only gradual (Fig. 2b,c and Supplementary Methods), whereas in others the mutual synchronization leads to a more abrupt improvement (Fig. 2d). Both scenarios are consistent with what is expected from theory and experiments in the literature on mutual synchronization of STNOs. The gradual case is predicted theoretically as a consequence of the weak coupling and varying difference in the free-running frequencies of two oscillators[28]. At the onset of synchronization, the relative phase is the largest with one of the oscillators trailing the other in phase.

If the free-running frequency of the slower oscillator has a stronger current dependence than the other, the relative phase will decrease with current, reach zero when the free-running frequencies coincide, then change sign, and eventually again reach a maximum negative value at the other synchronization boundary. Both the power and the linewidth of the mutually synchronized state are direct functions of the relative phase such that the power (linewidth) shows a maximum (minimum) when the relative phase crosses zero. In the case of non-crossing intrinsic frequencies, the relative phase will never reach zero, but still varies with the intrinsic frequency difference, with an optimum power and linewidth when the relative phase has a minimum.

One may notice a substantial increase in power fluctuations in the mutually synchronized state (for example, column III in Fig. 2), which to a lesser extent also seems present in the single nanoconstriction (Fig. 2a). This might be related to slow frequency jitter, 1/f noise, or otherwise coloured noise, on timescales similar to the data acquisition of the spectrum analyser, and with frequency deviations greater than the intrinsic linewidth[39–42]. We note that the appearance of large power fluctuations correlates with a narrow linewidth, which corroborates this picture. When we average four scans (Supplementary Figs 2–4) the power fluctuations are greatly reduced.

To learn more about the observed mutual synchronization, we have carried out micromagnetic simulations of double nanoconstrictions in a tilted magnetic field (Fig. 3). The two simulated nanoconstrictions differed in width by 8 nm, to mimic the natural variation of the fabrication process. We first simulated each nanoconstriction separately (Fig. 3a). The narrower SHNO shows an earlier onset of the auto-oscillations as a function of current, consistent with the higher current density. More importantly, the experimentally observed overall trend of the frequency first redshifting, then showing a minimum, and finally blueshifting with increasing current, is well reproduced by the simulations. To better understand what governs this behaviour we show the spatial profiles of the auto-oscillations in the insets of Fig. 3a. We find that the auto-oscillations emerge from the edges of the nanoconstrictions, similar to what has been reported for nanoconstriction and nanowire SHNOs[24,25,35,43] in in-plane fields.

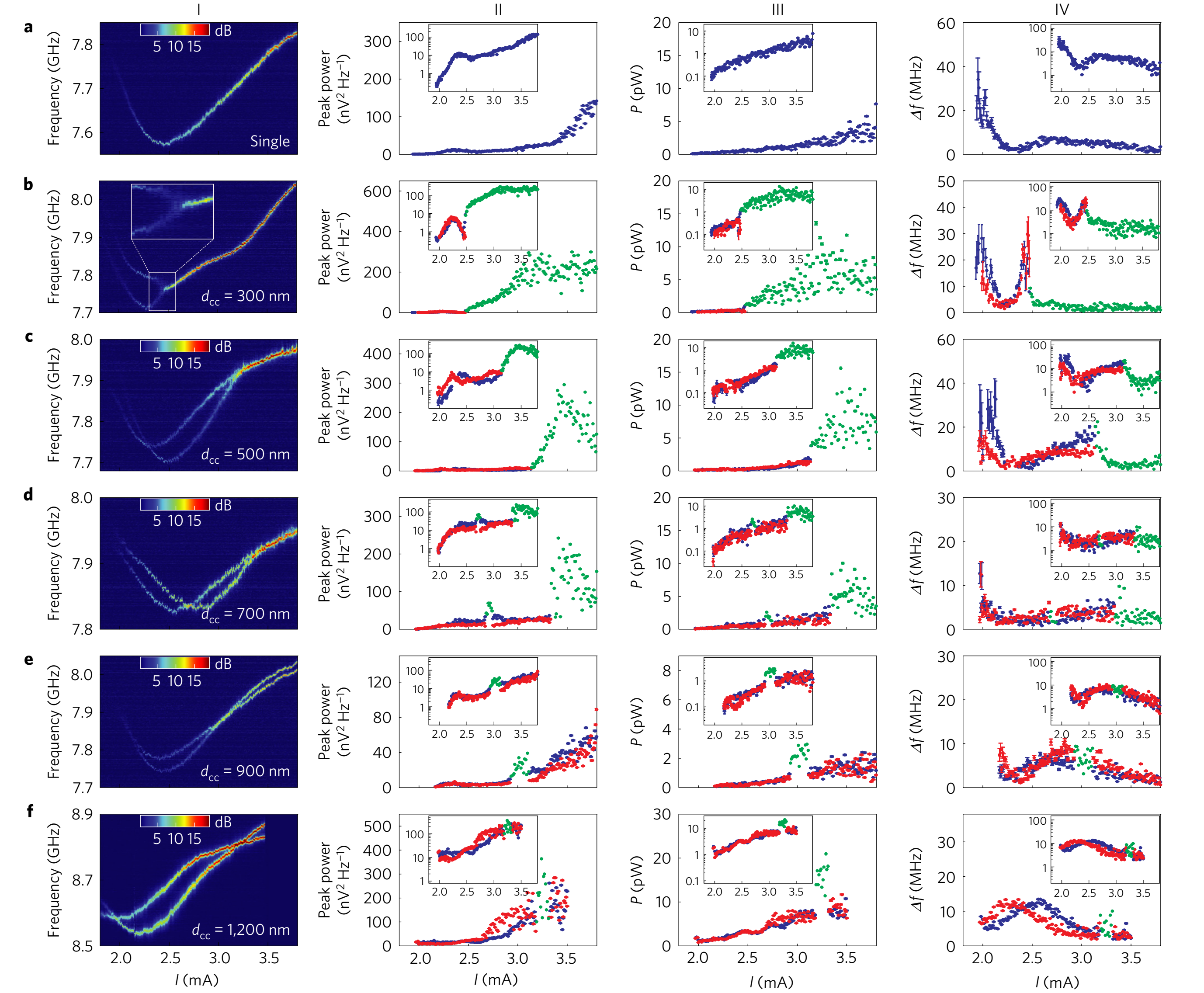

Figure 2 | Electrical microwave characterization. Results of a single nanoconstriction (**a**), and double nanoconstrictions with W = 120 nm and separated by d_{cc} = 300 nm (**b**), d_{cc} = 500 nm (**c**), d_{cc} = 700 nm (**d**), d_{cc} = 900 nm (**e**) and d_{cc} = 1,200 nm (**f**), in an applied field of 720 mT along $\varphi = 24°$ and $\theta = 80°$. The inset in **b** shows a zoom of the synchronization region. Column I gives the power spectral density versus current of the SHNO devices. Column II gives the microwave peak power density versus current of the signal in column I. Column III gives the total microwave power versus current of the signal. Column IV gives the Lorentzian linewidth versus current. Columns II and III show a sharp increase of the peak power and the total microwave power, respectively, as the two nanoconstrictions synchronize. A substantial improvement of the linewidth upon synchronization is shown in column IV.

However, in our case of out-of-plane fields, the auto-oscillation region expands into the nanoconstriction with increasing current, and the point of maximum intensity moves inwards. Consequently, the mode experiences a strongly varying field landscape such that the net effect is a frequency redshift as the mode leaves the edges, followed by a blueshift as it further expands into the bridges connecting the nanoconstrictions. The response of the simultaneously excited pair of nanoconstrictions is shown in Fig. 3b. At low current, the auto-oscillations are virtually indistinguishable from the individual simulations, suggesting a vanishing interaction between the auto-oscillating regions in this regime. However, as these regions expand at intermediate current, their mutual interaction can be observed both as substantial inter-modulation and as a gradual reduction of their frequency difference. Further mode expansion at higher current leads to stronger interaction, which finally makes the two modes synchronize at about 2.5 mA.

In the mutually synchronized state, only a single constant amplitude signal is generated (Fig. 3c), and the relative phase between the two nanoconstrictions remains constant over time (Fig. 3d). In contrast, the unsynchronized state is characterized by an amplitude that exhibits a steady beating (Fig. 3c), and a continuously varying relative phase (Fig. 3d). Figure 3e shows fast Fourier transforms (FFTs) and spatial maps of the two states, with mutual synchronization characterized by a single peak and both nanoconstrictions sharing the same spectral content, and the unsynchronized state showing two distinct peaks, each generated by one of the two nanoconstrictions. The rightmost inset in Fig. 3e shows a map of the instantaneous phase of all precessing spins in the synchronized state. One can clearly see two separate regions, each having its own phase, and an S-shaped boundary between those two regions where the phase changes continuously from the value of one region to the other. The phase map indicates that the interaction between the auto-oscillating regions takes place at this boundary and is mediated by direct exchange.

We can also confirm both the electrical and the simulated results using scanning micro-focused Brillouin light scattering microscopy

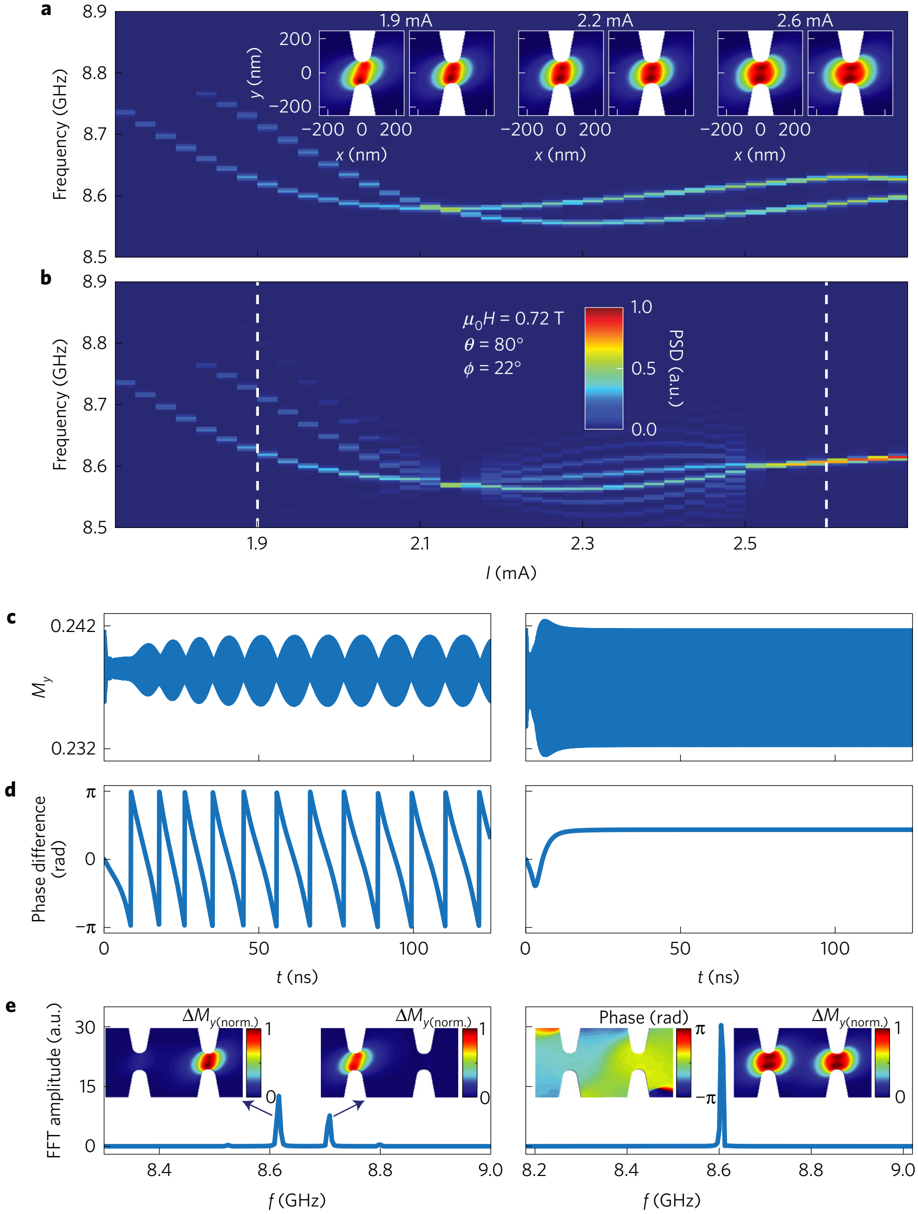

Q.3

Figure 3 | Micromagnetic simulations. a,**b**, Power spectral density versus current of the double free-running (**a**) and interacting (**b**) nanoconstriction SHNOs with the widths, ~~W,~~ of 117 nm and 125 nm and a separation of $d_{cc} = 500$ nm in an applied field of 720 mT along the $\varphi = 22°$ and $\theta = 80°$ direction. Q.4 The insets organized pairwise in **a** show the spatial distribution of the power spectral density of the auto-oscillations at the selected currents demonstrating the expansion of the corresponding modes as the applied current increases. The left and right panels in the pairs correspond to the larger and smaller nanoconstrictions, respectively. **c**, Averaged magnetization oscillation in time domain taken at 1.9 mA (left panel) and 2.6 mA (right panel). **d**, Phase difference between the two nanoconstriction. **e**, ~~Power spectral density~~ of the M_y component of the magnetization taken at 1.9 mA and 2.6 mA respectively. The colour plots in the insets present the spatial distribution of the spin wave amplitudes in the unsynchronized state (left) and the spin wave amplitude and phase in the synchronized state (right).

(μ-BLS)[4,5]. Figure 4 shows two rows of spin wave maps on the same device as inFig. 2d. The upper row corresponds to an unsynchronized state, whereas the bottom row shows similar maps in the mutually synchronized state. Since the spectral resolution of μ-BLS is insufficient to resolve the actual linewidth of the microwave signals and their separation in the unsynchronized state (Fig. 4b), we do not expect maps of the two states to look very different from each other. This is confirmed in column III in Fig. 4a, where maps for the two states show little qualitative difference. However, as all counts are binned into separate spin wave frequencies we can focus on the high and low ends of the μ-BLS peak, and plot spatial maps of the frequency-selected μ-BLS counts; maps at lower spin wave frequencies are shown in columns I & II, and maps at higher spin wave frequencies in columns IV & V. We then clearly see that whereas the maps of the mutually synchronized state do not change other than in their overall intensity, the maps of the unsynchronized state change entirely, indicating how the spin waves in the two nanoconstrictions have different frequencies. At the lowest mapped frequency there are essentially no counts in the lower nanoconstriction, and at the highest mapped frequency there are very few counts in the upper nanoconstriction. This is further quantified in Fig. 4e, where we plot the fraction of counts in the upper and lower halves of the maps for both the synchronized and non-synchronized case. Clearly, the relative counts do not change in the synchronized state, implying that their spectral spin wave content in both nanoconstrictions is identical. Interestingly, in the

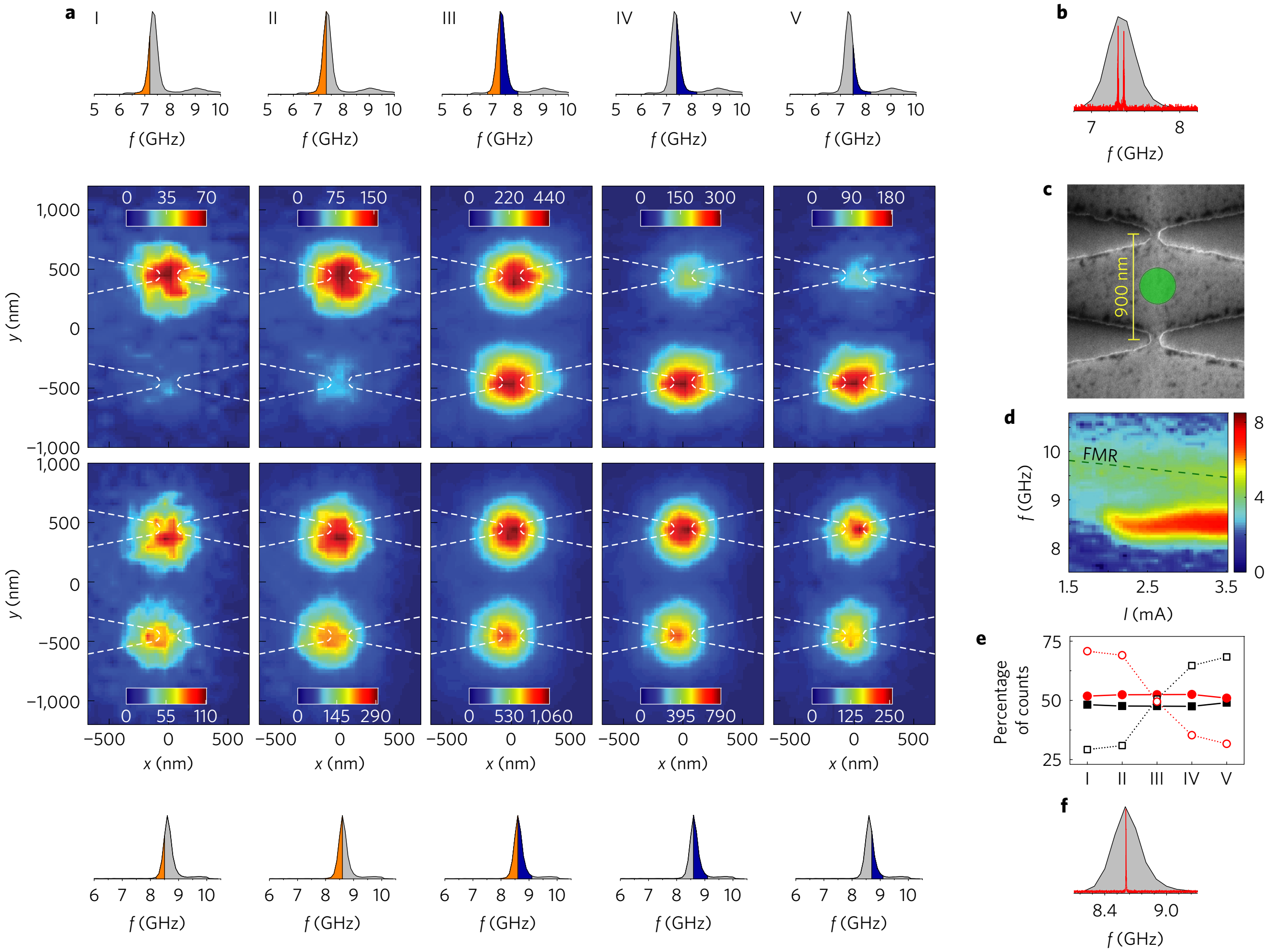

Figure 4 | μ-BLS measurements. a, Columns I–V show spatial maps of the μ-BLS counts in the unsynchronized (upper maps) and synchronized (lower maps) state, with a frequency selection indicated by the coloured regions in the spectra above and below each panel. **b**, The electrically measured microwave signal (red) overlaid on top of the total μ-BLS spectrum in the unsynchronized state, taken at a current of $I_{\mathrm{d.c.}} = 2.6$ mA and in a field of 553 mT along $\theta = 80°$ and $\varphi = 3°$. **c**, SEM picture of the SHNO. **d**, Spectra of the μ-BLS (logarithmic scale) as a function of the applied current as measured at the centre of the sample $x = y = 0$ (green spot in **c**), in a field of 640 mT, again along $\theta = 80°$ and $\varphi = 3°$ the FMR frequencies have a small negative slope due to the Oersted field (reinforced with the green dashed line as a guide to the eye). **e**, Fraction of the counts in the upper (circles) and lower (squares) half of the synchronized (filled symbols) and unsynchronized (open symbols) state, respectively. **f**, The electrically measured microwave signal (red) and total μ-BLS spectrum in the synchronized state, taken at a current of $I_{\mathrm{d.c.}} = 3.5$ mA and the same conditions as in **d**.

space between the constrictions, $x = y = 0$ as shown in Fig. 4c, a measurable intensity of spin waves is detected (Fig. 4d). We note that these excitations exhibit frequencies below the local ferromagnetic resonance (FMR; the FMR frequencies have a small negative slope due to the Oersted field created by the current running through the Pt layer) and are significantly more intense, consistent with auto-oscillations. The direct observation of finite excitations between the nanoconstrictions corroborates our micromagnetic simulations and suggests that direct exchange promotes the observed mutual synchronization. The observed upper limit of 1.2 µm for the mutual synchronization of two SHNOs is probably a consequence of damping in the bridge connecting the two nanoconstrictions. If so, it should be possible to further extend the maximum range of mutual synchronization by reducing the damping in the bridge. This can in principle be achieved through the same spin Hall effect driving the auto-oscillations in the nanoconstrictions[44–46]. By reducing the width of the bridge, and hence the current spread, we should be able to hold the local current density just below the auto-oscillation threshold and greatly enlarge the distance that the auto-oscillating regions can drive sub-threshold precession between the nanoconstrictions. Figure 5a shows the electrical microwave signal of such a double-SHNO device where two 140 nm nanoconstrictions, separated by 4 µm, are connected by a bridge that only opens up about 5°, Fig. 5c. When a current less than 2.6 mA is driven through the device, two individual microwave signals appear. When the current is further increased, the two signals merge, the power increases, and the linewidth ~~improves~~ (see Supplementary Section B and Supplementary Fig. 3), all strong indications that the two SHNOs have indeed synchronized over a distance as great as 4 µm. We expect that as the current is increased the auto-oscillating regions would expand towards the centre of the connecting bridge as the points where the local current density reaches the auto-oscillation threshold move inwards. Figure 5b plots μ-BLS line scans along the nanoconstrictions centre, x direction of the device, and clearly demonstrates that the auto-oscillating regions actually expand inwards, whereas their outer boundaries remain static. The approximately linear current dependence of the expansion also reflects the linear profile of the width of the bridge. Figure 5c shows a spatial μ-BLS map of the device in the same field and at a current of 2.4 mA. It is clear from the map that the auto-oscillation regions reside close to the nanoconstrictions, but inside the connecting bridge. In a device with 4 µm nanoconstriction

NATURE PHYSICS DOI: 10.1038/NPHYS3927

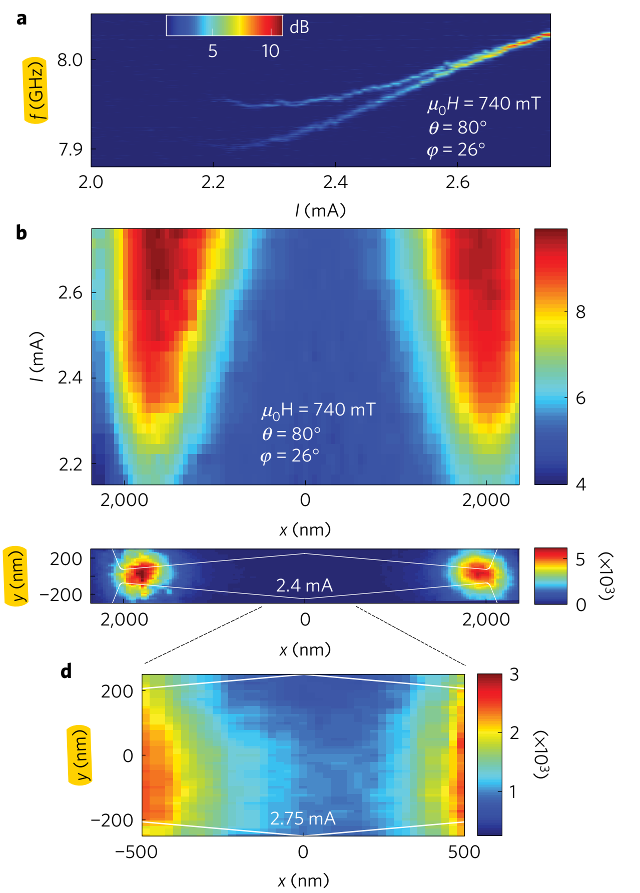

Figure 5 | Long-range synchronization. a, Power spectral density versus current of two 140 nm nanoconstrictions separated by 4 μm in an applied field of 740 mT along $\varphi = 26°$ and $\theta = 82°$. **b**, μ-BLS line scans (logarithmic scale) through the centre of the device at increasing currents. **c**, μ-BLS spatial map of the same device in the same field and at an applied current of 2.4 mA. **d**, μ-BLS scans through the central part of the device at 2.75 mA.

separation, the actual separation of the centres of the two oscillating regions is hence slightly reduced to about 3.7 μm. For a drive current of 2.75 mA—that is, in the synchronized state—we clearly find a non-zero amplitude of precession in the middle of the bridge on the same frequency as the two auto-oscillation regions (Fig. 5d). The long-range nature of the mutual synchronization hence appears to be a combined effect of both reduced damping and the two auto-oscillation regions approaching each other at high current.

Having demonstrated the ability to synchronize two oscillators over large distances, we now focus on how many more oscillators we can mutually synchronize. We fabricated SHNOs with multiple nanoconstrictions ranging from two to eleven with a fixed centre-to-centre separation of 300 nm. The largest number of mutually synchronized nanoconstriction we have observed is nine (Fig. 6); other examples of three and nine nanoconstrictions are shown in the Supplementary Methods. Although the overall synchronization behaviour is similar to that of double nanoconstrictions, we now also observe partially synchronized states. As shown in Fig. 6a, for low drive currents, each individual nanoconstriction generates its own separate microwave signal whose frequency first decreases with current. As each nanoconstriction passes its minimum frequency, their mutual interactions increase, promoting first a partially synchronized state, probably among neighbouring oscillators, which eventually leads to a globally synchronized state at about 3.29 mA. The maximum power in this regime reaches 54 pW—that is, significantly higher than the sum of the output powers of the free-running oscillators, but still less than the theoretical maximum increase of $N^2 = 81$, which indicates a finite relative phase difference between the individual oscillators. We also find that the nine mutually synchronized nanoconstrictions exhibit the lowest linewidth of about 2 MHz. For an accurate comparison between different numbers of nanoconstrictions we use the results from the averaged scans in the Supplementary Methods to mitigate the large scatter[40] observed in Fig. 2. Comparing linewidths at 3 mA we find about 10 MHz for single nanoconstrictions (Supplementary Fig. 1), 5 MHz for double nanoconstrictions (Supplementary Fig. 2), and 3–4 MHz for a triple nanoconstriction (Supplementary Fig. 4). This approximately inverse dependence on the number of nanoconstrictions is consistent with a total mode volume that grows linearly with the number of mutually synchronized nanoconstrictions mitigating the effect of the thermal fluctuations[47,48].

It is interesting to note that if we reduce the applied field substantially from 745 mT to 576 mT (Fig. 6g), while keeping the field direction about the same, we can no longer realize a mutually synchronized state. Instead, we mainly see individual signals, which redshift over a much larger current range. As the weaker field leads to a smaller out-of-plane angle of the magnetization, this corroborates our earlier conclusion that a certain minimum out-of-plane magnetization angle is required to drive the mode expansion, make the mode leave the nanoconstriction edge, and finally promote strong interaction between neighbouring oscillators. In other words, the applied field controls both the dispersion of the frequencies and the interaction between the oscillators.

To further verify the mutual synchronization of all nine nanoconstrictions, μ-BLS is utilized to spatially map both a synchronized (Fig. 6d–f), and an unsynchronized (Fig. 6g–i) state, of the same device as shown in Fig. 6a–c. In the synchronized state, the μ-BLS maps confirms that all nine nanoconstrictions have both the same frequency and similar amplitudes (Fig. 6e,f). Since our diffraction limited resolution (360 nm) cannot resolve the individual oscillators with 300 nm centre-to-centre spacing, the nine oscillators appear as a continuous auto-oscillating region. However, micromagnetic simulations still confirm that the synchronized state consists of nine individual auto-oscillating regions interacting via their evanescent tails. In contrast, the μ-BLS map of the unsynchronized, or possibly partially synchronized state, shows a varying frequency along the connected nanoconstrictions, with some possible clustering of neighbouring oscillators, which might indicate partial or pairwise synchronization.

It is noteworthy that the total power is on par with typical ~~GMR~~ based devices, despite the much lower AMR, which indicates that Q.5 the coherent ~~SW~~ power in the synchronized SHNOs is very high. Q.6 Although the microwave power is still orders of magnitude lower than that of magnetic tunnel junction (MTJ)-based STNOs, which can surpass 2 μW (ref. 49), we expect three terminal SHNO devices Q.7 to perform even better. In such devices, mutually synchronized SHNOs would generate the SW power, and MTJs, fabricated on top of each oscillating region, would convert these SWs into microwave power. As the drive current path and the MTJ current paths can then be optimized individually, MTJs with much higher tunnelling magnetoresistance could be used instead of today's low-resistance-area MTJ-based STNOs, providing yet another increase in power.

Although mutual synchronization is an important step towards meeting the power and phase noise requirements of commercial applications, our demonstration of robust synchronization over very large distances, and for a large number of nanoconstrictions, also opens up additional intriguing possibilities in magnon spintronics[50] and spin wave computing[51–54]. Whereas all nanoconstrictions in this work were placed on a single line, we expect more complex nanoconstriction arrangements to also operate successfully and show synchronization. One may, for example, envisage spin wave

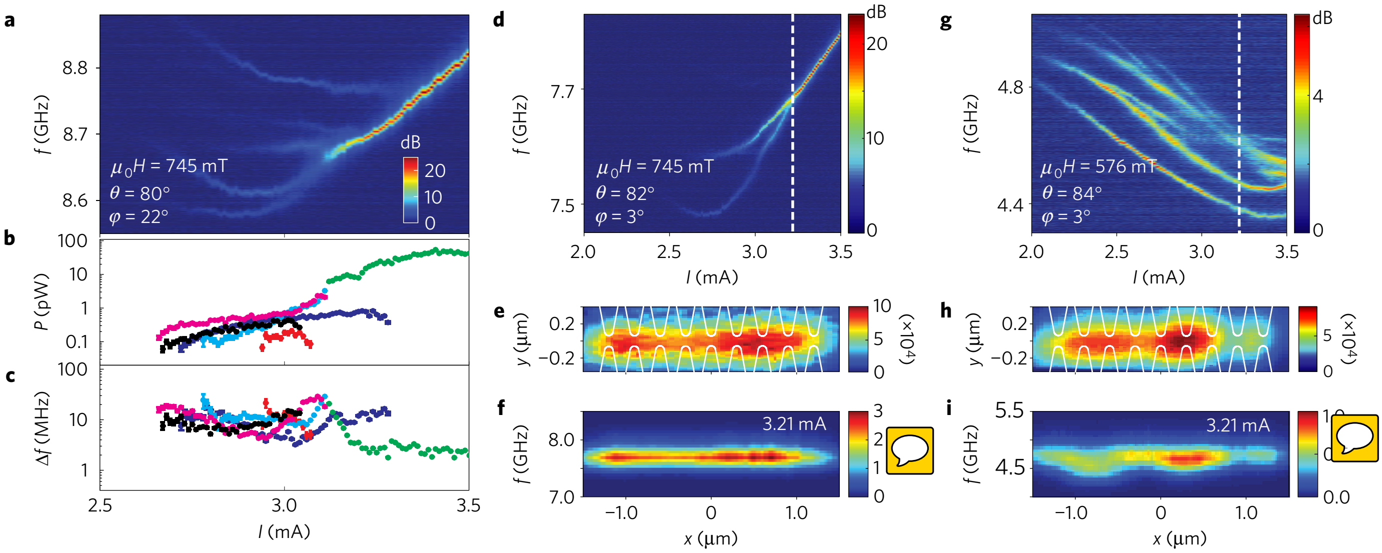

Figure 6 | Multiple SHNO synchronization. a, Power spectral density versus current of the SHNO in Fig. 1, with nine nanoconstrictions with ~~W~~ = 120 nm ~~width each~~ separated by d_{cc} = 300 nm from each other, in an applied field of 745 mT along $\varphi = 22°$, and $\theta = 80°$. **b**, Total power of the extracted individual peaks and the globally synchronized peak. **c**, Linewidth of the extracted peaks. **d**, Power spectral density versus current of the SHNO in an applied field of 745 mT along $\varphi = 3°$ and $\theta = 82°$. **e**, μ-BLS spatial map taken at synchronization $I_{\cancel{\mathrm{d.c.}}}$ = 3.21 mA. **f**, μ-BLS frequency map of the central horizontal line passing through all nanoconstrictions, at $y = 0$. **g**, Power spectral density versus current of the SHNO in an applied field of 576 mT along $\varphi = 3°$ and $\theta = 84°$. **h**, μ-BLS spatial map taken at $I_{\cancel{\mathrm{d.c.}}}$ = 3.21 mA. **i**, μ-BLS frequency map of the central horizontal line passing through all nanoconstrictions, at $y = 0$.

majority gates[52,54] where three or more smaller nanoconstrictions are connected to a larger nanoconstriction such that they all operate at the same current density and approximately the same frequency. When driven into mutual synchronization, the phase of the output nanoconstriction will then acquire the majority phase value of the inputs. Wave computing can also be used in oscillatory neural networks, and as neural synchronization has been demonstrated to govern associative memory processes[55], SHNO networks with tunable coupling strengths may mimic neurons in the brain[56].

The relative ease of fabrication of strongly synchronized nanoconstriction SHNOs will hence enable the design and fabrication of more complex and highly networked nanoconstriction-based architectures where both digital and analog spin-wave-based computing can be realized.

Methods

Methods, including statements of data availability and any associated accession codes and references, are available in the online version of this paper.

Received 19 May 2016; accepted 16 September 2016;
published online XX Month XXXX

References

1. Slonczewski, J. C. Current-driven excitation of magnetic multilayers. *J. Magn. Magn. Mater.* **159,** L1–L7 (1996).
2. Berger, L. Emission of spin waves by a magnetic multilayer traversed by a current. *Phys. Rev. B* **54,** 9353–9358 (1996).
3. Ralph, D. & Stiles, M. Spin transfer torques. *J. Magn. Magn. Mater.* **320,** 1190–1216 (2008).
4. Demidov, V. E., Urazhdin, S. & Demokritov, S. O. Direct observation and mapping of spin waves emitted by spin-torque nano-oscillators. *Nat. Mater.* **9,** 984–988 (2010).
5. Madami, M. *et al*. Direct observation of a propagating spin wave induced by spin-transfer torque. *Nat. Nanotech.* **6,** 635–638 (2011).
6. Tsoi, M. *et al*. Generation and detection of phase-coherent current-driven magnons in magnetic multilayers. *Nature* **406,** 46–48 (2000).
7. Rippard, W., Pufall, M., Kaka, S., Russek, S. & Silva, T. Direct-current induced dynamics in $Co_{90}Fe_{10}/Ni_{80}Fe_{20}$ point contacts. *Phys. Rev. Lett.* **92,** 027201 (2004).
8. Silva, T. & Rippard, W. Developments in nano-oscillators based upon spin-transfer point-contact devices. *J. Magn. Magn. Mater.* **320,** 1260–1271 (2008).
9. Bonetti, S., Muduli, P., Mancoff, F. & Åkerman, J. Spin torque oscillator frequency versus magnetic field angle: the prospect of operation beyond 65 GHz. *Appl. Phys. Lett.* **94,** 102507 (2009).
10. Bonetti, S. *et al*. Experimental evidence of self-localized and propagating spin wave modes in obliquely magnetized current-driven nanocontacts. *Phys. Rev. Lett.* **105,** 217204 (2010).
11. Bonetti, S. & Åkerman, J. Nano-contact spin-torque oscillators as magnonic building blocks. *Top. Appl. Phys.* **125,** 177–187 (2013).
12. Urazhdin, S. *et al*. Nanomagnonic devices based on the spin-transfer torque. *Nat. Nanotech.* **9,** 509–513 (2014).
13. Dumas, R. *et al*. Recent advances in nanocontact spin-torque oscillators. *IEEE Trans. Magn.* **50,** 4100107 (2014).
14. Slonczewski, J. Excitation of spin waves by an electric current. *J. Magn. Magn. Mater.* **195,** 261–268 (1999).
15. Kalinikos, B. A. & Slavin, A. N. Theory of dipole-exchange spin wave spectrum for ferromagnetic films with mixed exchange boundary conditions. *J. Phys. C* **19,** 7013–7033 (1986).
16. Hoefer, M., Silva, T. & Stiles, M. Model for a collimated spin-wave beam generated by a single-layer spin torque nanocontact. *Phys. Rev. B* **77,** 144401 (2008).
17. Dumas, R. K. *et al*. Spin-wave-mode coexistence on the nanoscale: a consequence of the Oersted-field-induced asymmetric energy landscape. *Phys. Rev. Lett.* **110,** 257202 (2013).
18. Madami, M. *et al*. Propagating spin waves excited by spin-transfer torque: a combined electrical and optical study. *Phys. Rev. B* **92,** 024403 (2015).
19. Hirsch, J. E. Spin Hall effect. *Phys. Rev. Lett.* **83,** 1834–1837 (1999).
20. Kato, Y. K., Myers, R. C., Gossard, A. C. & Awschalom, D. D. Observation of the spin Hall effect in semiconductors. *Science* **306,** 1910–1913 (2004).
21. Sinova, J., Valenzuela, S. O., Wunderlich, J., Back, C. H. & Jungwirth, T. Spin Hall effects. *Rev. Mod. Phys.* **87,** 1213–1260 (2015).
22. Demidov, V. E. *et al*. Magnetic nano-oscillator driven by pure spin current. *Nat. Mater.* **11,** 1028–1031 (2012).
23. Liu, R. H., Lim, W. L. & Urazhdin, S. Spectral characteristics of the microwave emission by the spin Hall nano-oscillator. *Phys. Rev. Lett.* **110,** 147601 (2013).
24. Duan, Z. *et al*. Nanowire spin torque oscillator driven by spin orbit torques. *Nat. Commun.* **5,** 5616 (2014).
25. Demidov, V. E., Urazhdin, S., Zholud, A., Sadovnikov, A. V. & Demokritov, S. O. Nanoconstriction-based spin-Hall nano-oscillator. *Appl. Phys. Lett.* **105,** 172410 (2014).
26. Ranjbar, M. CoFeB-based spin Hall nano-oscillators. *IEEE Magn. Lett.* **5,** ~~1–4~~ (2014).

27. Langenfeld, S. *et al*. Exchange magnon induced resistance asymmetry in permalloy spin-Hall oscillators. *Appl. Phys. Lett.* **108** (2016).

28. Slavin, A. & Tiberkevich, V. Nonlinear auto-oscillator theory of microwave generation by spin-polarized current. *IEEE Trans. Magn.* **45,** 1875–1918 (2009).

29. Mancoff, F. B., Rizzo, N. D., Engel, B. N. & Tehrani, S. Phase-locking in double-point-contact spin-transfer devices. *Nature* **437,** 393–395 (2005).

30. Kaka, S. *et al*. Mutual phase-locking of microwave spin torque nano-oscillators. *Nature* **437,** 389–392 (2005).

31. Pufall, M., Rippard, W., Russek, S., Kaka, S. & Katine, J. Electrical measurement of spin-wave interactions of proximate spin transfer nanooscillators. *Phys. Rev. Lett.* **97,** 087206 (2006).

32. Sani, S. *et al*. Mutually synchronized bottom-up multi-nanocontact spin-torque oscillators. *Nat. Commun.* **4,** 2731 (2013).

33. Houshang, A. *et al*. Spin-wave-beam driven synchronization of nanocontact spin-torque oscillators. *Nat. Nanotech.* **11,** 280–286 (2016).

34. Demidov, V. E. *et al*. Synchronization of spin Hall nano-oscillators to external microwave signals. *Nat. Commun.* **5,** 3179 (2014).

35. Kendziorczyk, T. & Kuhn, T. Mutual synchronization of nanoconstriction-based spin Hall nano-oscillators through evanescent and propagating spin waves. *Phys. Rev. B* **93,** 134413 (2016).

36. Slavin, A. N. & Kabos, P. Approximate theory of microwave generation in a current-driven magnetic nanocontact magnetized in an arbitrary direction. *IEEE Trans. Magn.* **41,** 1264–1273 (2005).

37. Slavin, A. & Tiberkevich, V. Spin wave mode excited by spin-polarized current in a magnetic nanocontact is a standing self-localized wave bullet.. *Phys. Rev. Lett.* **95,** 237201 (2005).

38. Consolo, G., Lopez-Diaz, L., Torres, L. & Azzerboni, B. Magnetization dynamics in nanocontact current controlled oscillators. *Phys. Rev. B* **75,** 214428 (2007).

39. Houssameddine, D. *et al*. Temporal coherence of MgO based magnetic tunnel junction spin torque oscillators. *Phys. Rev. Lett.* **102,** 257202 (2009).

40. Devolder, T. *et al*. Auto-oscillation and narrow spectral lines in spin-torque oscillators based on MgO magnetic tunnel junctions. *J. Appl. Phys.* **106,** 103921 (2009).

41. Keller, M., Pufall, M., Rippard, W. & Silva, T. Nonwhite frequency noise in spin torque oscillators and its effect on spectral linewidth. *Phys. Rev. B* **82,** 1–8 (2010).

42. Eklund, A. *et al*. Dependence of the colored frequency noise in spin torque oscillators on current and magnetic field. *Appl. Phys. Lett.* **104,** 092405 (2014).

43. Yang, L. *et al*. Reduction of phase noise in nanowire spin orbit torque oscillators. *Sci. Rep.* **5,** 16942 (2015).

44. Demidov, V. E., Urazhdin, S., Rinkevich, A. B., Reiss, G. & Demokritov, S. O. Spin Hall controlled magnonic microwaveguides. *Appl. Phys. Lett.* **104,** 152402 (2014).

45. An, K. *et al*. Control of propagating spin waves via spin transfer torque in a metallic bilayer waveguide. *Phys. Rev. B* **89,** 140405 (2014).

46. Evelt, M. *et al*. High-efficiency control of spin-wave propagation in ultra-thin yttrium iron garnet by the spin-orbit torque. *Appl. Phys. Lett.* **108,** 172406 (2016).

47. Kim, J.-V., Tiberkevich, V. & Slavin, A. Generation linewidth of an auto-oscillator with a nonlinear frequency shift: spin-torque nano-oscillator. *Phys. Rev. Lett.* **100,** 1–4 (2008).

48. Tiberkevich, V. S., Slavin, A. N. & Kim, J.-V. Temperature dependence of nonlinear auto-oscillator linewidths: application to spin-torque nano-oscillators. *Phys. Rev. B* **78,** 092401 (2008).

49. Maehara, H. *et al*. Large emission power over 2 μW with high Q factor obtained from nanocontact magnetic-tunnel-junction-based spin torque oscillator. *Appl. Phys. Exp.* **6,** 113005 (2013).

50. Chumak, A. V., Vasyuchka, V. I., Serga, A. A. & Hillebrands, B. Magnon spintronics. *Nat. Phys.* **11,** 453–461 (2015).

51. Khitun, A., Bao, M. & Wang, K. L. Magnonic logic circuits. *J. Phys. D* **43,** 264005 (2010).

52. Khitun, A. & Wang, K. L. Non-volatile magnonic logic circuits engineering. *J. Appl. Phys.* **110,** 034306 (2011).

53. Macià, F., Kent, A. D. & Hoppensteadt, F. C. Spin-wave interference patterns created by spin-torque nano-oscillators for memory and computation. *Nanotechnology* **22,** 095301 (2011).

54. Klingler, S. *et al*. Design of a spin-wave majority gate. *Appl. Phys. Lett.* **105,** 152410 (2014).

55. Fell, J. & Axmacher, N. The role of phase synchronization in memory processes. *Nat. Rev. Neurosci.* **12,** 105 (2011).

56. Locatelli, N., Cros, V. & Grollier, J. Spin-torque building blocks. *Nat. Mater.* **13,** 11–20 (2013).

Acknowledgements

We thank M. Madami for assistance in building the μ-BLS microscope. This work was supported by the European Research Council (ERC) under the European Community's Seventh Framework Programme (FP/2007-2013)/ERC Grant 307144 'MUSTANG'. This work was also supported by the Swedish Research Council (VR), the Swedish Foundation for Strategic Research (SSF), and the Knut and Alice Wallenberg Foundation.

Author contributions

A.A.A. designed the devices. P.D. and A.H. fabricated the devices. A.A.A., P.D. and A.H. performed all electrical measurements. R.K.D. and A.A.A. built the μ-BLS microscope. A.A.A. carried out all optical measurements. A.A.A. and M.D. performed the micromagnetic simulations. All authors contributed to the data analysis and co-wrote the manuscript.

Additional information

Supplementary information is available in the online version of the paper. Reprints and permissions information is available online at www.nature.com/reprints. Correspondence and requests for materials should be addressed to J.A.

Competing financial interests

The authors declare no competing financial interests.

Methods

Sample fabrication. A bilayer of 6 nm Pt and 5 nm Py ($Ni_{80}Fe_{20}$) was magnetron sputtered in a system with a base pressure lower than 3×10^{-8} ~~torr~~ at room temperature onto a 20 mm × 20 mm piece of sapphire C-plane substrate, and then *in situ* covered with 5 nm SiO_2 to prevent the permalloy layer from oxidation. The bilayer was then patterned into 4 µm × 12 µm rectangles with different bow-tie-shaped constrictions by e-beam lithography and subsequent argon ion milling using negative e-beam resist as the etching mask. The devices were then covered with an additional 50 nm SiO_2 layer to protect them from oxidation during measurements. A coplanar waveguide provides electrical contacts and is defined by optical lithography, reactive ion etching of the protective SiO_2 layer, sputtering of copper, and lift-off.

Electrical characterization. All measurements were performed at room temperature. We mounted the sample with a fixed in-plane angle on a rotatable sample holder between the poles of an electromagnet. The current bias was applied through a high-frequency bias-T and the resulting radiofrequency oscillations amplified by a low-noise amplifier and recorded with a high-frequency spectrum analyser using a low-resolution bandwidth of 300 kHz. Figure 2 shows single scan data to minimize the time the device spends at high current. All other electrical microwave measurements (Fig. 6 and Supplementary Methods) are from four averaged scans at each current, which reduces the scatter substantially. The obtained spectra were corrected to correspond to the power emitted by the device, taking into account the amplifier gain, the losses from the radiofrequency components and cables, and the impedance mismatch between the device and the 50 Ω measurement line. The spectra were fitted with a single symmetric Lorentzian to extract the auto-oscillation frequency, power and linewidth.

μ-BLS characterization. The magneto-optical measurements were performed using room-temperature micro-focused BLS measurements. Spatially resolved maps of the magnetization dynamics are obtained by focusing a polarized monochromatic 532 nm single-frequency laser (solid state diode-pumped) using a high numerical aperture (NA = 0.75) dark-field objective, which yields a diffraction limited resolution of 360 nm. The scattered light from the sample surface is then analysed by a high-contrast six-pass Tandem Fabry–Perot interferometer TFP-1 (JRS Scientific Instruments). The obtained BLS intensity is proportional to the square of the amplitude of the magnetization dynamics at the corresponding frequency. The μ-BLS set-up is equipped with a spectrum analyser connected to the sample via bias-T to measure the electrical and the optical signals simultaneously.

Micromagnetic simulations. The micromagnetic simulations were done using the graphics processor unit (GPU)-based finite-difference micromagnetic solver MuMax3 (ref. 57). The SHNO is modelled by 1,024 × 1,024 × 1 cells with a cell size of $3.9063 \times 3.9063 \times 5\,\mathrm{nm}^3$. The parameters used in the simulation include the saturation magnetization $\mu_0 M_s = 0.754\,\mathrm{T}$, exchange stiffness $A_{ex} = 10 \times 10^{-12}\,\mathrm{J\,m^{-1}}$, and the damping constant $\alpha = 0.022$, all determined from experiments on blanket films. In addition to the applied field $H = 0.72\,\mathrm{T}$, the charge current distribution and the resulting Oersted field landscape is calculated using COMSOL Multiphysics simulation software (www.comsol.com). The corresponding spin current is then calculated from the simulated charge current in the Pt layer (see, for example, Fig. 1c) and converted into a SHE-generated spin current in the $-\hat{z}$-direction assuming a spin Hall angle, $J_S/J_C = \theta_{SH} = 0.08$. The spin Hall angle is also determined experimentally from the same bilayer using spin-torque-induced ferromagnetic resonance (ST-FMR) on a 1-µm-wide stripe, a measurement similar to that performed in ref. 58 and found to be $\theta_{SH} = 0.08 \pm 0.01$ in our bilayer system. The spin current is approximated to have a 100% spin polarization along the $-\hat{x}$-direction. The auto-oscillation frequency is obtained by performing the FFT of the simulated time evolution (250 ns total) of the averaged magnetization after an initial 60 ns of transient behaviour is disregarded. By performing a discrete Fourier transform of each simulation cell, a full spatial map of the generated auto-oscillations is extracted. The free-running oscillators are modelled one by one in the full-scale pair geometry by suppressing the spin current density on either smaller or larger nanoconstriction sites. This allows for a direct comparison with the response of the simultaneously acting (interacting) oscillators.

Data availability. The data that support the plots within this paper and other findings of this study are available from the corresponding author upon reasonable request.

References

57. Vansteenkiste, A. *et al*. The design and verification of MuMax3. *AIP Adv.* **4,** 107133 (2014).
58. Liu, L., Moriyama, T., Ralph, D. C. & Buhrman, R. A. Spin-torque ferromagnetic resonance induced by the spin Hall effect. *Phys. Rev. Lett.* **106,** 036601 (2011).

Queries for NPG paper nphys3927

Page 1

Query 1:
The phrase 'for the first time' has been deleted here as per instruction from NPG.

Page 2

Query 2:
Please check x-axis label in Figure 1c is correct. There appear to be multiple versions.

Page 4

Query 3:
Differences were found between the two versions of figures 3e (y axis label and values) and 5c (values of colour scale bar) supplied. Please check that the correct version has been followed in each case.

Query 4:
Panels b,c,d changed to c,d,e in Figure 3 caption.

Page 6

Query 5:
Please define/expand GMR, used only once.

Query 6:
Please define SW, used only in this paragraph.

Query 7:
Please note that reference numbers are formatted according to style in the text, so that any reference numbers following a symbol or acronym are given as 'ref. XX' on the line, whereas all other reference numbers are given as superscripts.

Page 7

Query 8:
Please give the article ID of refs 5, 41 and 47 (the page ranges given look as though they are internal only).

Page 8

Query 9:
Please provide page range/article id for ref. 27.

Query 10:
Please provide final page number of the range for refs 43 and 55 (if the numbers already provided are article numbers, no action is required).

Query 11:
A.A. changed to A.A.A. in the Author Contribution section, to match the name listed on the first page. Please check.